Microstructure and Properties of Well-Ordered Multiferroic $Pb(Zr,Ti)O_3/CoFe_2O_4$ Nanocomposites

Xingsen Gao,[†,‡,*] Brian J. Rodriguez,[†] Lifeng Liu,[†] Balaji Birajdar,[†] Daniel Pantel,[†] Michael Ziese,[§] Marin Alexe,[†] and Dietrich Hesse[†]

[†]Max Planck Institute of Microstructure Physics, D-06120 Halle (Saale), Germany, [‡]School of Physics and Telecommunication Enginering, South China Normal University, 510006, Guangzhou, China, and [§]Division of Superconductivity and Magnetism, University of Leipzig, D-04103 Leipzig, Germany

ABSTRACT A nanofabrication technique combining pulsed laser deposition and a nanoporous anodic aluminum oxide membrane mask is being proposed to prepare various types of multiferroic nanocomposites, *viz.* periodically ordered $CoFe_2O_4$ dots covered by a continuous $Pb(Zr,Ti)O_3$ layer, $Pb(Zr,Ti)O_3$ dots covered with $CoFe_2O_4$, and $Pb(Zr,Ti)O_3/CoFe_2O_4$ bilayer heterostructure dots. By properly tuning the processing parameters, epitaxial nanodot-matrix composites can be obtained. For the composite consisting of $CoFe_2O_4$ nanostructures covered by a $Pb(Zr,Ti)O_3$ film, an unexpected out-of-plane magnetic easy axis induced by the top $Pb(Zr,Ti)O_3$ layer and a uniform microdomain structure can be observed. The nanocomposites tested by piezoresponse force microscopy (PFM) exhibit strong piezoelectric signals, and they also display magnetoelectric coupling revealed by magnetic-field dependent capacitance measurement.

KEYWORDS: multiferroics · AAO template · nanodot array · magnetoelectric coupling · nanocomposite

The past few years have witnessed a renaissance of research interests in magnetoelectric multiferroics, a family of materials that display both electric and magnetic order simultaneously.[1−8] Multiferroics are not only promising for multifunctional devices in which a single element performs multiple tasks, but also bring about a completely new device paradigm *via* the mutual coupling between their dual order parameters, for example, for magnetoelectric sensors or data storage.[7] The resurgence in multiferroic research has led to numerous breakthroughs that pave the way to applications of these materials.[7] However, the application of single phase multiferroics ("intrinsic multiferroics") is still very limited as none of them displays reasonably large electrical and magnetic polarization simultaneously at room temperature. An alternative approach is to construct composite materials, for example, laminate multilayers and other three-dimensional composites,[9−12] which have reached magnetoelectric coupling coefficients three to five orders larger than those of intrinsic multiferroics and thus are approaching the threshold of technical applications. Special attention should be paid to the discovery of a self-organized columnar composite such as $BaTiO_3-CoFe_2O_4$, $CoFe_2O_4-BiFeO_3$, or $CoFe_2O_4-PbTiO_3$,[12−15] in which the segregation of two immiscible components has led to a self-assembled nanopillar and matrix structure. Such composites can achieve larger magnetoelectric coupling at room temperature than most single-phase multiferroics and even allow switching of the magnetization by an electric field. The magnetoelectric properties of these composites are related to the strain transferred from the phase boundaries and, thus, are critically dependent on their geometry on the nanoscale. For instance, a relatively simple stain field distribution may be favorable for developing a good coupling. Therefore, it is of great interest to explore composites with simpler strain field by creating various predesigned structures as a strategy for searching for new candidates with promising properties. In spite of various efforts attempting to tailor the structure and properties of these composites,[13−15] control and design of such heterostructures still remain a challenge.

In this work, a process that combines pulsed laser deposition (PLD) and an ultrathin nanoporous anodic aluminum oxide (AAO) membrane as stencil mask has been applied to fabricate regularly arranged $CoFe_2O_4-PbZr_{0.2}Ti_{0.8}O_3$ (CFO-PZT) nanocomposites of various combinations, *viz.* periodically ordered nanodot arrays of one type of material embedded into a matrix of a continuous film of another material or bilayered heterostructure dots. CFO is chosen for its good magnetic properties and low conductivity, and especially for its large

*Address correspondence to gaoxingsen@gmail.com.

Received for review September 25, 2009 and accepted January 18, 2010.

Published online January 29, 2010.
10.1021/nn9012934

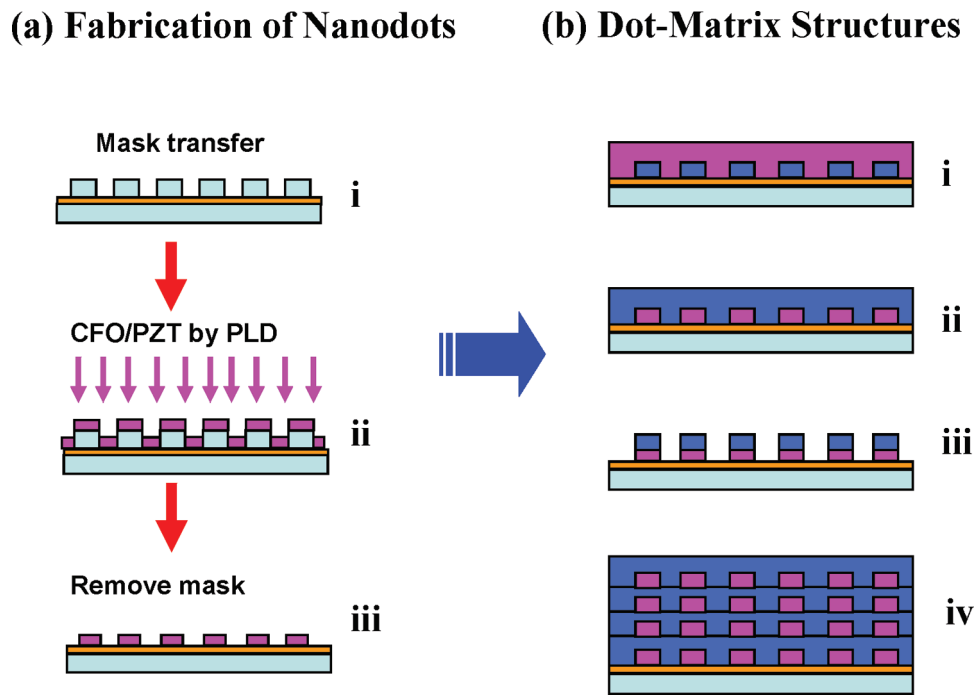

Figure 1. (a) Schematic flowcharts of the fabrication procedure of periodical nanodot structures: (i) transfer of the AAO membrane mask to the SRO/STO substrate, (ii) deposition of the material (CFO or PZT) through the mask, (iii) removal of the mask, obtaining the nanodot structures. (b) Schematic illustration of the dot-matrix (continuous film) structure of the two components (PZT, red; CFO, blue): CFO (dot)-PZT (matrix) dot-matrix nanostructure (i); PZT (dot)-CFO (matrix) structure (ii); heterostructured PZT-CFO nanodot array (iii); complex three-dimensional multiple layers of dot-matrix structures of PZT (dot)-CFO (matrix) or CFO (dot)-PZT (matrix) (iv).

magnetorestriction, and has been widely used to construct composite multiferroics. PZT, with the chosen composition, exhibits excellent ferroelectric and piezoelectric properties with square hysteresis loops, and due to our experience, it is possible to achieve defect-free structures with uniform ferroelectric domains within this material. The attempt to combine the above two components in regular arrays may lead to a new family of composite materials with novel physical properties and enable the nanometer-scale tailoring of such structures and their properties in a controlled manner.

RESULTS AND DISCUSSION

Microstructures of Various Types of Dot-Matrix Composites.

The dot-matrix composite nanostructures are fabricated using a combination of PLD and AAO mask involving two major steps: the preparation of the ordered nanodot array and the deposition of a continuous film to form various matrix structures as schematically illustrated in Figure 1. The details of the fabrication procedure of periodically ordered nanodot arrays can be found in Experimental Methods as well as in previous reports.[16−18] In brief, it involves three steps, as illustrated in Figure 1a: AAO mask transfer (i), materials deposition by PLD (ii), and removal of mask. After the fabrication of the nanodots, another constituent in form of dots or a film was deposited again by PLD to form nanocomposites, according to the predesigned structures. The substrates used here are (100)-oriented $SrTiO_3$ (STO) or MgO substrates coated with a conducting $SrRuO_3$ (SRO) layer as bottom electrode for electric characterization. An example of a mask used in this work is shown in the Supporting Information, Figure S1a, and the periodical dot array after removal of the mask is illustrated in Figure S1b. We are demonstrating here the concepts of different types of dot-matrix structures in Figure 1b, *viz.* CFO dots covered by PZT (i), PZT dots covered by CFO (ii), and bilayered dot arrays (iii), as well as more complex multiple dot-matrix structures with both components (iv), by depositing PZT and CFO through pulsed laser deposition according to the respective predesigned structure. It is worth noting that the matrix films on top of the dots do not show flat top surfaces, as expected, instead there remains a certain extent of periodicity of the underneath nanostructures, which will be further addressed below.

The AAO masks used here include almost periodically ordered circularly shaped holes, which are well-ordered over distances of a few micrometers. Really perfectly ordered AAO membranes with long-range ordered nanodot arrays could also be achieved by incorporation of a preimprint process, allowing for the fabrication of perfectly ordered structures.[19−21] This technique also enables further adjusting the periodical structures, *e.g.*, the dot sizes and interdot distances. By varying hole size and periodicity of the AAO template, the lateral size of the nanodot array can be varied from 30 to 300 nm with an interdot

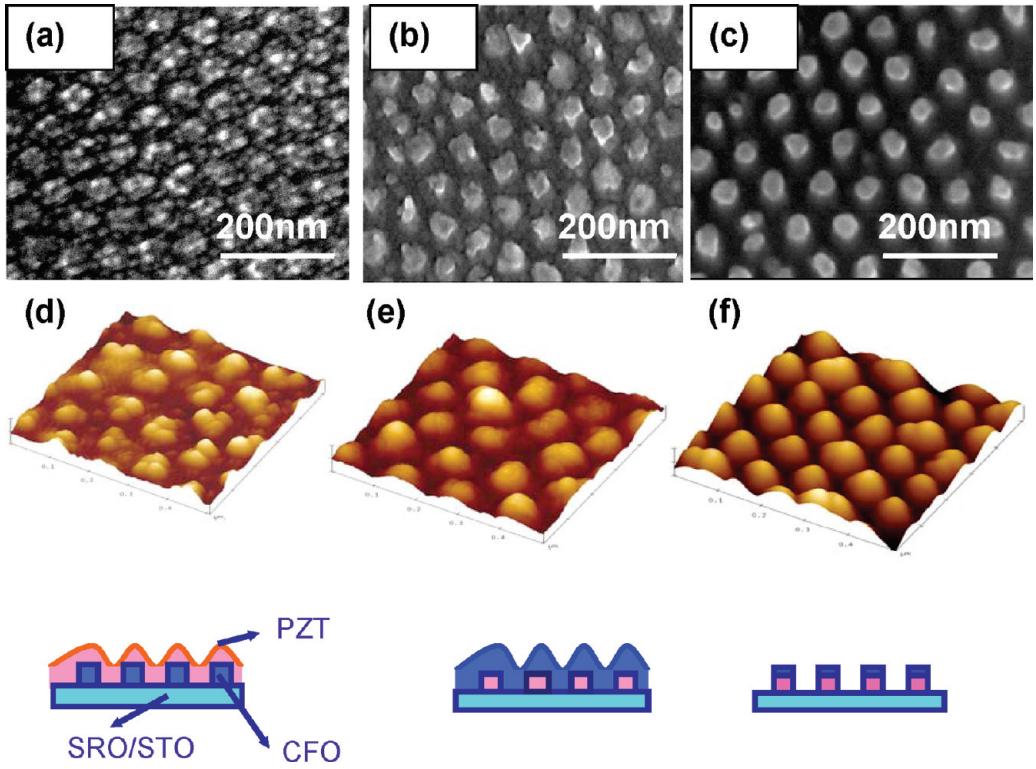

Figure 2. SEM and AFM images for the three types of multiferroic composites on (100)-orientated SRO/STO substrates: CFO dots covered by a continuous layer of PZT (a,d); PZT dots covered by a continuous layer of CFO (b,e); heterostructured bilayer nanodot array of CFO/PZT (c,f). The inserts below the images show the corresponding schematic diagrams of geometric configurations for the predesigned composites.

distance ranging from 60 to 500 nm.[16,22,23] In comparison to the self-assembly nanodot-matrix structures developed by Zheng *et al.*,[12,13] the present method gives a large freedom in tailoring the composites (dot size, dot density, periodicity, pattern symmetry, *etc.*) as well as the physical properties in a controlled manner as a method of nanostructure engineering.

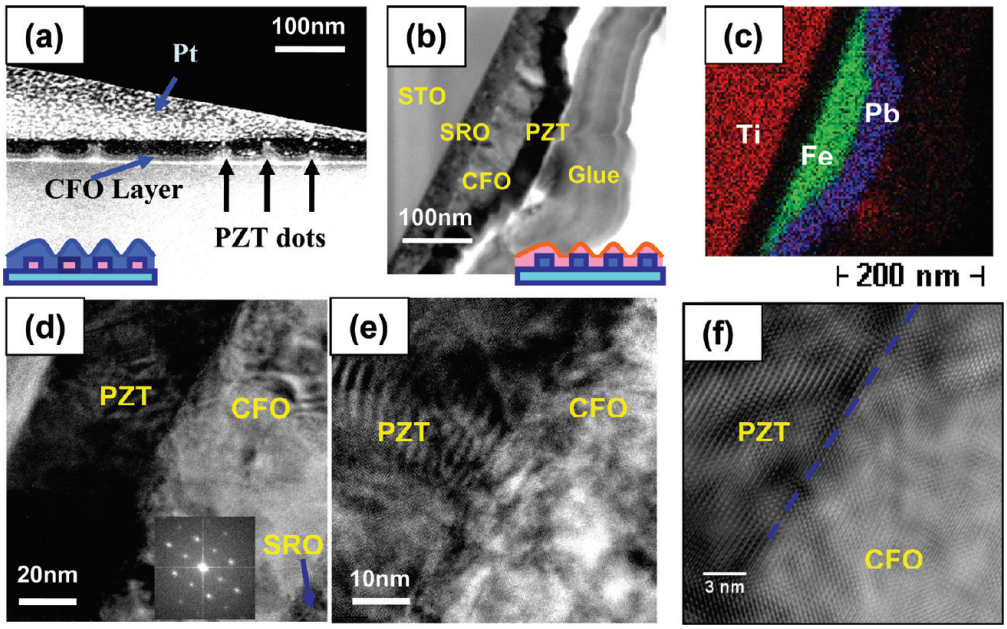

Figure 3. (a) Cross-section SEM image of the PZT dots covered by a continuous CFO film (the sample was prepared by FIB). (b,c) Cross-section TEM image of the CFO dot array covered by a PZT film (the TEM sample was prepared by a conventional mechanical thinning and ion milling process), *viz.* low resolution TEM bright field image (b) and the corresponding chemical compositional mapping (c). (d−f) HRTEM images of the same sample as (b) at three different magnifications. The inset in (d) is the fast Fourier transform pattern (FFT).

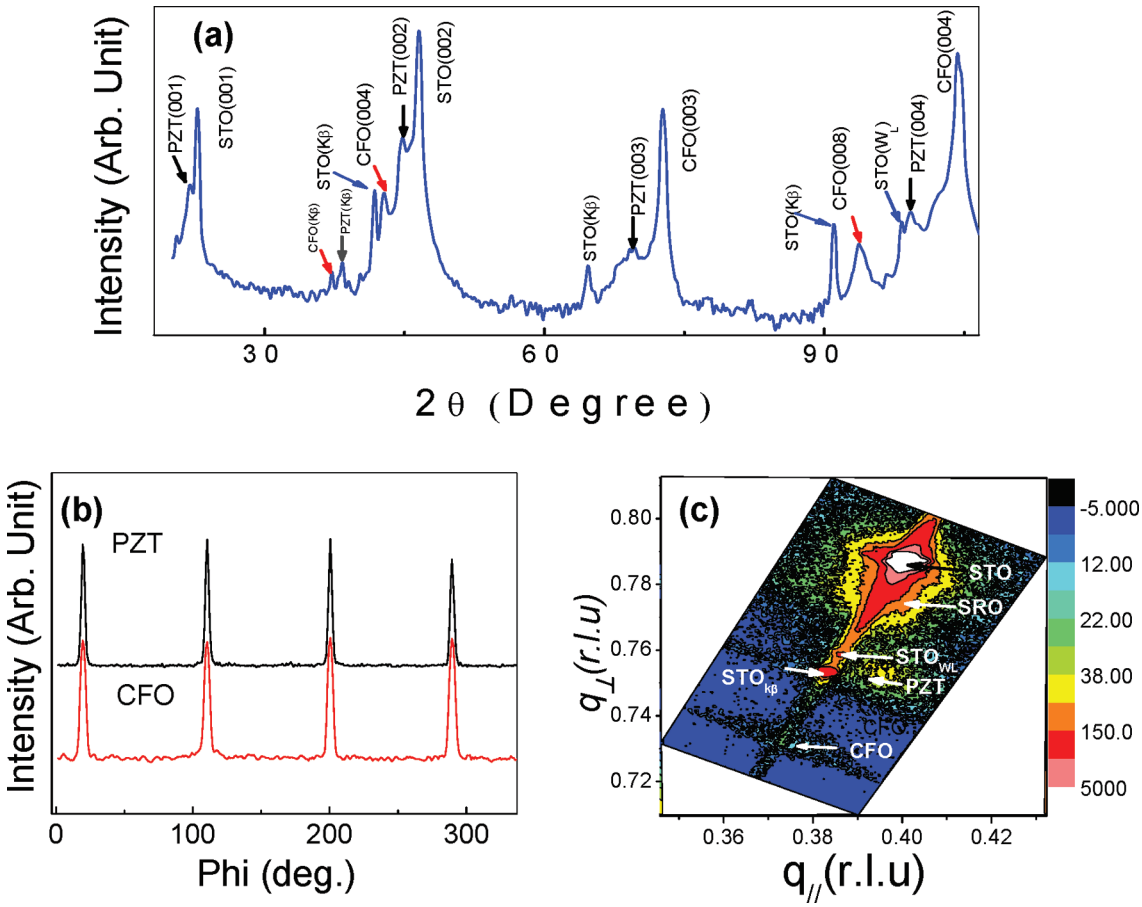

Figure 4. XRD diffraction pattern for the epitaxial CFO nanodot array (diameter: ~290 nm, height: ~70 nm) covered by a layer of PZT (50 nm thick) obtained at a high deposition temperature of 500 °C and an oxygen pressure of 0.05 mbar: θ−2θ scan (a), and Φ-scan (b) of the CFO (110) peak, indicating a cube-on-cube growth of CFO on SRO. Reciprocal space mapping (*c*) around the STO (204) reflection further confirms the epitaxial growth of CFO.

By using different combinations of AAO template and deposited materials, we are able to obtain various nanodot (core) and continuous film (matrix) composites. Three examples of these predesigned composites are shown by SEM and AFM images in Figure 2: (a,d) a CFO dot array covered with a continuous PZT film (CFO (dot)/PZT (film)); (b,e) PZT dots covered with a CFO film (PZT (dot)/CFO (film)); and (c,f) CFO-PZT heterostructured bilayer dots. As shown in Figure 1a,b, the as-prepared composites exhibit ordered morphologies of nanodot arrays similar to those of the underneath dots. The above dot-film composites show a periodically ordered structure with a lateral size of ~50 nm and inter-dot distance of ~100 nm. For the bilayer PZT/CFO dots (Figure 2c,f), well-defined periodically ordered nanodots are observed, and the dot height can reach as much as 100 nm derived from the depth profile of the AFM surface image (Figure S2c). From the top-view and tilted SEM images, the CFO capping layer displays a cone-like structure (Figures S2a,b), probably due to the gradual shrinkage of the hole size during deposition.

Cross-section samples of the as-prepared nanocomposites were studied by SEM and (S)TEM. Figure 3a shows an SEM image of part of a PZT (dot)/CFO (film) composite. From this image, one can easily identify the embedded dot-film matrix structure in which the PZT dots show cone-like shapes and are nearly uniformly covered by a continuous CFO layer, giving rise to a periodical morphology on its top surface. Figure 3b is a cross-section image obtained from a CFO (dot)/PZT (film) composite with lateral dot size of ~300 nm. The CFO dots were deposited at an oxygen pressure of 0.05 mbar and a temperature of 500 °C to ensure their epitaxial growth, and the PZT layer was deposited at an oxygen pressure of 0.2 mbar and a temperature of 575 °C. From the bright field image, we are able to identify the contrast between the different layers, *viz.* SRO layer, CFO dot, and PZT layer. To evaluate the compositional distribution and look for potential interfacial diffusion, EDX compositional mapping was performed. As shown in Figure 3c, the chemical distribution map shows the different layers consistent with the predesign of the structures, *viz.* CFO dot and PZT layer. The distribution of the individual elements is also shown in the Supporting Information, Figure S3a, in which the elements are well confined to their respective structure. The lattice structure was examined by HRTEM at different magnifications, as shown in Figure 3d−f. The individual layers

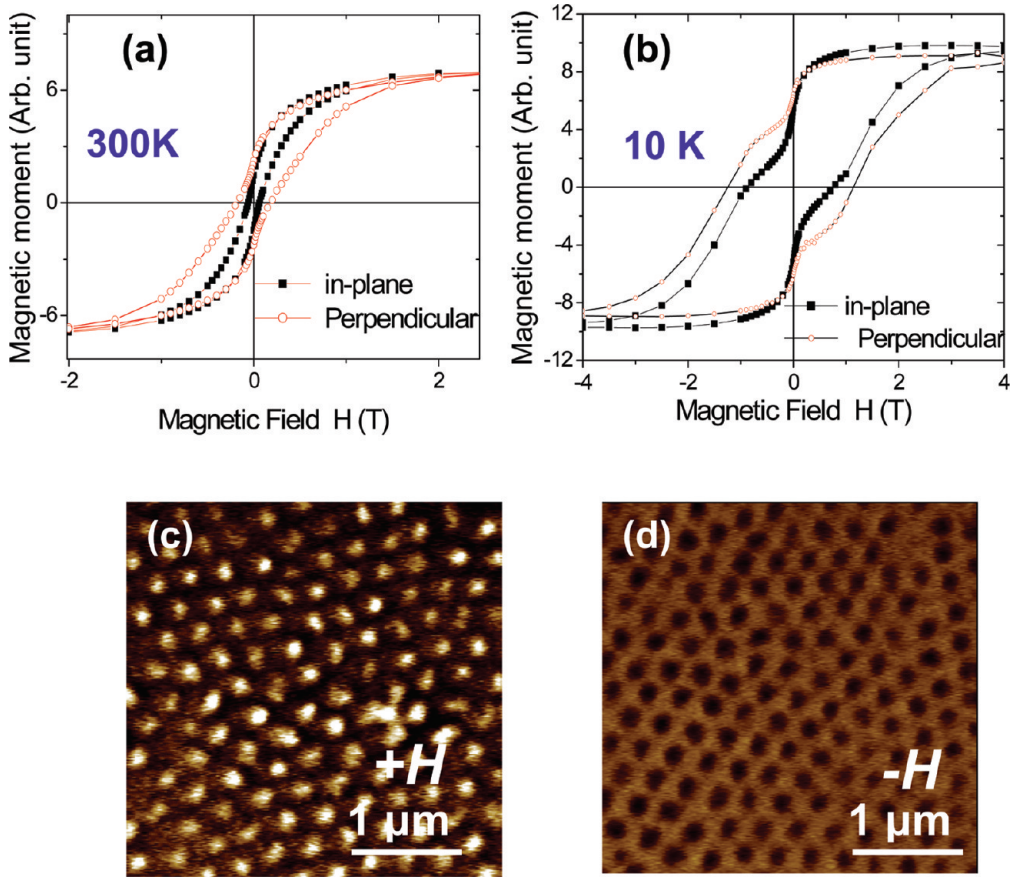

Figure 5. Hysteresis loops for the CFO nanodot array on SRO electrode, covered by a layer of PZT, with an average dot diameter of ~300 nm and dot height of ~70 nm, measured by SQUID at magnetic field along both in-plane and perpendicular directions, at room temperature (a) and at 10 K (b). MFM images for the nanodot array at remanence state that have been premagnetized by a field (*H*) along perpendicular direction (*c*) and by a reverse field (−*H*) along the opposite direction (d).

of SRO, PZT, and CFO show different contrasts, and epitaxial growth is demonstrated by the fast Fourier transform (FFT) inserted in Figure 3d. A lattice image of a region close to the CFO/PZT interface is shown in Figure 3f, indicating the formation of a well-established crystal lattice.

Epitaxial Structure for a CFO (Dot)/PZT (Film) Composite. The structure of the CFO (dot)/PZT (film) composite was further examined by X-ray diffraction, as shown in Figure 4. As visible in the θ−2θ scan plotted in Figure 4a, the diffraction peaks from CFO (004) and (008) and PZT (001), (002), (003), (004) can be well indentified among other peaks from the substrate, such as STO K_α-, K_β-, and W_L-related peaks. No impurities, foreign phases, or orientations other than the *c*-axis orientation can be found. The epitaxial relation was further verified by a Φ-scan (Figure 4b), using the (110) diffraction spot, in which four sharp peaks can be found in both the PZT and the CFO diffraction patterns, indicating a well-established cube-on-cube epitaxial growth of both the dots and the film on the STO substrate. A reciprocal space map (RSM) of the CFO/PZT structure close to the STO (204) diffraction peak (along $q_\parallel$ and $q_\perp$) is shown in Figure 4c, where $q_\parallel$ and $q_\perp$ are the reciprocal coordinates with a reciprocal lattice unit (r.l.u.) of λ/2*d*, where λ is the X-ray wavelength and *d* is the lattice plane spacing. The RSM displays weak CFO and PZT diffraction spots along with other strong diffractions from the STO substrate. PZT shows only a single spot corresponding to the *c*-axis-oriented domains ("*c*-domains"); no detectable traces of *a*-domains can be found. The diffraction spot from CFO is rather weak and diffuse along the *x*-axis, indicating a considerable extent of lattice strain relaxation along the *a*-axis.

Magnetic Properties. In this work, our main focus is to show that the combined PLD and AAO template mask technique is an effective way to create various ferroelectric/magnet structures and that the latter can possess multiferroic properties. The functional properties of one example (CFO (dot)/PZT (film)) will be shown explicitely, whereas a systematic investigation of the properties of the structures of other types will be carried out in future work. The magnetic properties of the CFO (dot)/PZT (film) composite were studied by superconducting quantum interference device (SQUID) magnetometry and magnetic force microscopy (MFM), see Figure 5. At room temperature, the isothermal magnetization shows well-established magnetization hyster-

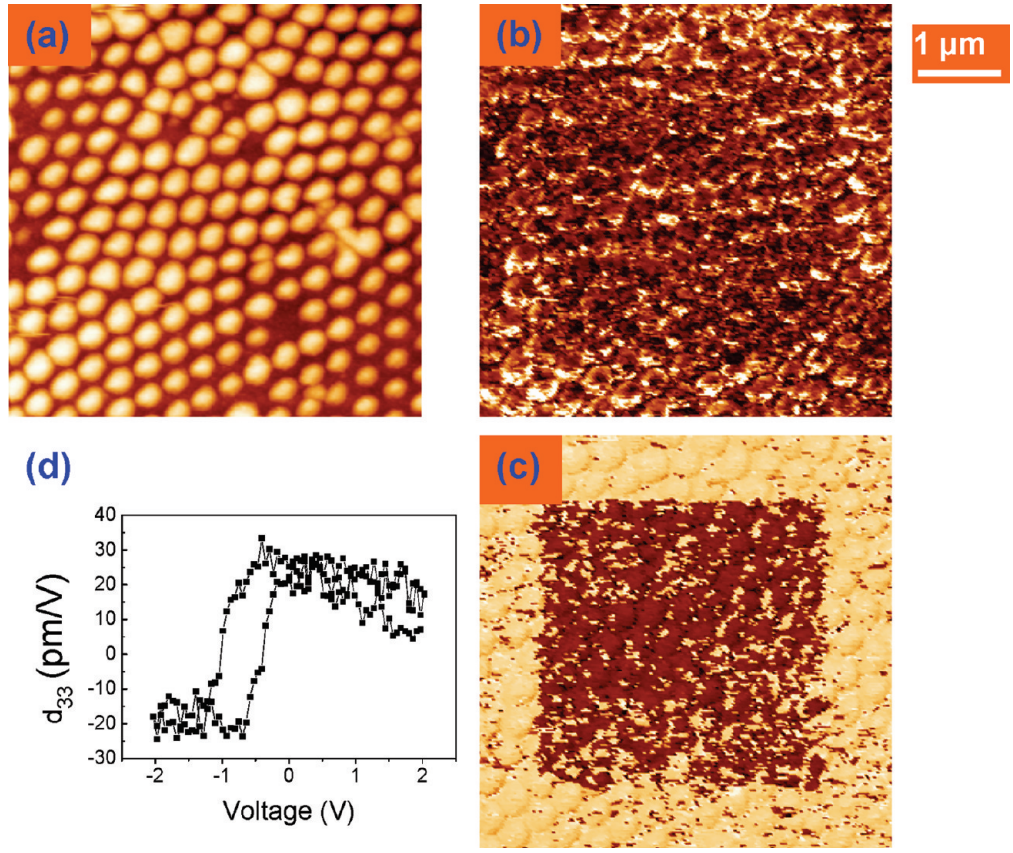

Figure 6. Piezoelectric force microscopy measurement of CFO dots covered by a PZT film: morphology (a), amplitude image for PFM response along the vertical direction (b), phase image for PFM response along the vertical direction (c), and d_{33} hysteresis loop (d). In the middle of the scanned area, a reverse voltage (−5 V) was applied leading to the contrast change in both amplitude and phase images.

esis loops (Figure 5a). Rounding of the curves leads to remanent magnetization values much smaller than the saturation magnetization due to the demagnetization process. It is not straightforward to deduct the easy-axis direction from these measurements. One might obtain one hint from the values of the coercive field: because this is larger in the perpendicular direction, one might, within a Stoner−Wohlfarth model,[24] argue that the magnetic easy axis is along the surface normal. This is corroborated by the MFM scans shown in Figure 5c,d, which indeed show a remanent switchable magnetic moment along the surface normal after magnetizing the sample in a large magnetic field either in the up or down direction. Further, the CFO dots appear to be in a single domain state.

The magnetic anisotropy in the CFO (dot)/PZT (film) composite is significantly different from that of both single layer CFO films and freestanding CFO dots. Whereas CFO films on $SrRuO_3$-buffered $SrTiO_3$ substrates show a stronger in-plane anisotropy,[25] bare CFO dots (see Figure S4b) do not show any distinctive uniaxial magnetic anisotropy (note that no shearing correction has been applied in Figure S4b). Cobalt ferrite films under tensile strain develop a perpendicular-to-plane easy axis due to the magnetoelastic coupling energy and a negative magnetostriction coefficient λ_{100},[26] whereas the same mechanism leads to an in-plane easy axis under compressive strain.[25] However, the results in ref 25 further show that these magnetoelastic energy considerations that depend on the assumption of a homogeneous strain distribution can lead to wrong predictions and that the actual growth morphology and strain distribution has to be taken into account. For an accurate prediction of the easy axis direction of the CFO (dot)/PZT (film) composite, one would have to take into account the three-dimensional strain distribution in the dots, which is beyond the scope of this paper. In our case, the out-of-plane magnetization can also be correlated to an additional stress field built up by the PZT layer. The mechanism for such a substantial increase of stress is still not very clear; it may be attributed to either lattice mismatch strain along the dot-matrix interface or to thermal expansion differences.

At low temperatures, as shown in Figure 5b for 10 K, a double transition develops in the magnetization hysteresis curves due to the ferromagnetism in the $SrRuO_3$ buffer layer. Magnetization sweeps *vs.* temperature curves presented in Figure S4a show a broad ferromagnetic transition of the $SrRuO_3$ layers below 145 K. The buffer layer was probably slightly deoxygenated due to the growth of the cobalt ferrite dots at the comparatively low pressure of 0.05 mbar.

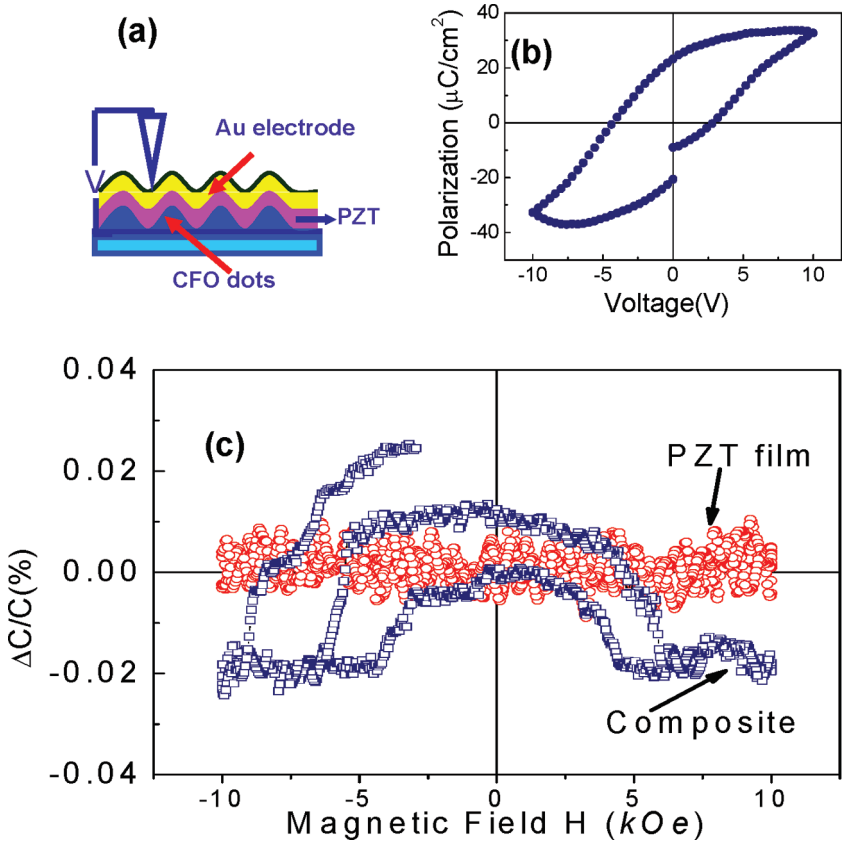

Figure 7. Measurement of the room-temperature magneto-capacitance for the CFO dots covered by a PZT layer. (a) Schematic diagram of the capacitor structure used for electrical measurements; (b) polarization hysteresis loop for a capacitor; and (c) capacitance as a function of magnetic field showing an apparent field dependence of the capacitance change. For comparison, the magneto-capacitance of a PZT film without CFO dots is also shown.

Ferroelectric Properties. The electromechanical properties of these nanoarray composites were further tested by piezoelectric force microscopic (PFM) studies, as shown in Figure 6, where out-of-plane piezoelectric response was observed. In the phase image, a rather uniform polarization could be observed for the as-deposited composite. After applying a reverse voltage of −5 V, the polarization could be well switched into the reverse direction, as indicated by the change of phase contrast in the polarized area. Polarization switching was further confirmed by a piezoelectric hysteresis loop, which is rather square, although it exhibits some extent of imprint indicated by a horizontal shift. It is also noted that the piezeoelectric signal directly above a CFO dot is slightly weaker than in the surrounding areas, which can be due to the field drop across the CFO dots.

Magnetoelectric Coupling. Finally, initial tests of the magnetoelectric (ME) coupling of the composites were performed at room temperature by help of a capacitance structure with Au as top electrodes, as schematically shown in Figure 7a. A typical macroscopic P-E hysteresis loop of the CFO (dot)/PZT (film) composite is shown in Figure 7b, displaying a rather large polarization of about 20 μC/cm^2, although the loop is somewhat leaky and indicates a high polarization relaxation. The ME effect was tested by measuring the change of capacitance as a function of external magnetic field. The capacitance exhibits a magnetic field-dependent behavior as show in Figure 7c. Although the induced capacitance is rather small (around 0.03% at 1 T), such field-dependent behavior is repeatable over several tests. To exclude any parasite effects from artifacts, a similar test was performed on a pure PZT film on SRO with the same testing parameters, and no detectable field-induced capacitance change was found. The origin of the magneto-capacitance is still not clear. It is likely due to the combination of magnetoelastic and piezoelectric effects through strain mediation.[10−12] In addition, interface conductivity, *e.g.*, Maxwell−Wagner effects, may also contribute to the induced capacitance.[27,28] Further studies are needed to understand the mechanism. In this work, the testing frequency of the magnetocapacitance measurement is 100 kHz, which is far beyond the space charge activation frequency. The observed magnetoelectric coupling is, thus, more likely a result of the strain field transfer between different phases.

The above results indicate that the present method is capable of fabricating multiferroic composites with long-range order and well-designed structures. By further improving the quality of the individual compo-

nents or a better design of the geometric configurations, it should be possible to further enhance the magnetoelectric coupling through a nanoscale engineering of the chemical and interfacial coupling.

CONCLUSION

In summary, a family of artificially designed multiferroic nanocomposites was successfully fabricated by using PLD and AAO templates. The presented method enables the fabrication of three-dimensional composites with predesigned geometric structure. By carefully controlling the deposition parameters, epitaxially grown composites can be obtained. The nanocomposites possess both electrical and magnetic properties with an apparent enhancement in out-of-plane anisotropy induced by the top PZT layer and also show a magnetoelectric coupling revealed by magnetocapacitance measurements.

EXPERIMENTAL METHODS

Fabrication Procedures for the Dot-Matrix Composites. The details of the fabrication procedure of periodically ordered nanodot arrays are illustrated in the schematic flowchart in Figure 1a. A conducting layer of $SrRuO_3$ was predeposited on the (100)-oriented $SrTiO_3$ (STO) or MgO substrates by pulsed laser deposition. An ultrathin AAO membrane with predefined, variable size of the holes was then transferred onto the substrate in a liquid environment. The membrane mask with self-organized periodically ordered pores had been prepared by an electrochemical anodizing technique, which has been described elsewhere.[17−20] The CFO material was deposited by PLD in an ambient pressure range from 10^{-5} bar to 0.05 mbar and at elevated temperatures ranging from 200 to 550 °C. Subsequently, the AAO mask was mechanically removed and thus an ordered dot array attached to the substrate was obtained. Finally, another constituent in form of dots or a film was deposited by PLD to form a nanocomposite, and the above procedure can be repeated to form more complex structures. Figure S1a is an example of a mask used in this work, and Figure S1b illustrates the periodical dot array after removal of the mask.

Characterizations of Structure and Properties. The crystal structure was characterized by X-ray diffraction using a Philips X'Pert MRD diffractometer with CuKα (λ = 1.54 Å) radiation. Magnetic properties were characterized by a superconducting quantum interference device (SQUID) magnetometer and a magnetic force microscope (MFM; SPM, DI 5000), which can also be used to record images of the surface morphology. Scanning electron microscopy (SEM) images were obtained by a JEOL JSM-6700F microscope. Transmission electron microscopy (TEM) investigations were conducted by a Philips CM20T (Philips, Netherlands) at a voltage of 200 kV and a HRTEM JEOL 4010 (JEOL, Japan) at 400 kV. Energy-dispersive X-ray analysis (EDX) maps were recorded in a scanning transmission electron microscope (STEM) of type Philips CM20FEG equipped with a field-emission gun, working at 200 kV. The samples for TEM were thinned either using mechanical and ion-beam based standard methods or using a dual-type focused ion beam (FIB) equipment of type FEI Nova 600 NanoLab. P-E hysteresis loops were measured by a TF Analyzer (aixACCT2000), and the magneto-capacitance measurement was performed by a HP4194 Impedance Analyzer that is connected to a low temperature cryogenic probe system equipped with a horizontal superconductor DC magnetic field (TTP-4-2, Lakeshore). Piezoelectric force microscopic (PFM) images were obtained by a commercially available atomic force microscope (AFM; TM Microscopes, AutoProbe CP Research) equipped with a lock-in amplifier (DSP7260, Signal Recovery) and a $PtIr_5$-coated conducting AFM tip (ATEC-EFM, Nanosensors) as also described elsewhere.[22]

Acknowledgment. Thanks are due to N. Schammelt for FIB thinning. Two of the authors (X.S.G and B.J.R) acknowledge the Alexander von Humboldt Foundation for financial support. This work was partially supported by German Science Foundation (DFG) *via* SFB 762. Professor D.H.B (Sun Yat-Sen University, Guangzhou, P.R. China) is acknowledged for technical support and most helpful discussions.

Supporting Information Available: Description of the detailed experimental procedures, and supplemental figures showing the AFM topology, EDX compositional maps, and magnetic properties of the nanostructured composites. This material is available free of charge *via* the Internet at http://pubs.acs.org.

REFERENCES AND NOTES

1. Ramesh, R.; Spaldin, N. A. Multiferroics: Progress and Prospects in Thin Films. *Nat. Mater.* **2007**, *6*, 21–29.
2. Eerenstein, W.; Mathur, N. D.; Scott, J. F. Multiferroic and Magnetoelectric Materials. *Nature* **2000**, *442*, 759–65.
3. Spaldin, N. A.; Fiebig, M. The Renaissance of Magnetoelectric Multiferroics. *Science* **2005**, *309*, 391–92.
4. Fiebig, M. Revival of the Magnetoelectric Effect. *J. Phys. D: Appl. Phys.* **2005**, *38*, R123−52.
5. Wang, K. F.; Liu, J. M.; Ren, Z. F. Multiferroicity: the Coupling Between Magnetic and Polarization Orders. *Adv. Phys.* **2009**, *58*, 321–448.
6. Eerenstein, W.; Wiora, M.; Prieto, J. L.; Scott, J. F.; Mathur, N. D. Giant Sharp and Persistent Converse Magnetoelectric Effects in Multiferroic Epitaxial Heterostructures. *Nat. Mater.* **2007**, *6*, 348–51.
7. Scott, J. F. Data Storage: Multiferroic Memories. *Nat. Mater.* **2007**, *6*, 256–57.
8. Cheong, S. W.; Mostovoy, M. Multiferroics: a Magnetic Twist for Ferroelectricity. *Nat. Mater.* **2007**, *6*, 13–20.
9. Nan, C.-W.; Bichurin, M. I.; Dong, S.-X.; Viehland, D.; Srinivasan, G. Multiferroic Magnetoelectric Composites: Historical Perspective, Status, and Future Directions. *J. Appl. Phys.* **2008**, *103*, 031101.
10. Nan, C.-W.; Gang., L.; Lin, Y.; Chen, H. Magnetic-Field-Induced Electric Polarization in Multiferroic Nanostructures. *Phys. Rev. Lett.* **2005**, *94*, 197203.
11. Zhai, J.; Xing., Z.; Dong, S.; Li, J.; Viehland, D. Magnetoelectric Laminate Composites: an Overview. *J. Am. Ceram. Soc.* **2008**, *91*, 351–58.
12. Zheng, H.; Wang, J.; Lofland, S. E.; Ma, Z.; Mohaddes-Ardabili, L.; Zhao, T.; Salamanca-Riba, L.; Shinde, S. R.; Ogale, S. B.; et al. Multiferroic $BaTiO_3$-$CoFe_2O_4$ Nanostructures. *Science* **2004**, *303*, 661–63.
13. Zheng, H. M.; Zhan, Q.; Zavaliche, F.; Sherburne, M.; Straub, F.; Cruz, M. P; Chen, L. Q.; Dahmen, U.; Ramesh, R. Controlling Self-Assembled Perovskite-Spinel Nanostructures. *Nano Lett.* **2006**, *6*, 1401–07.
14. Zavaliche, F.; Zheng, H.; Mohaddes-Ardabili, L.; Yang, S. Y.; Zhan, Q.; Shafer, P.; Reilly, E.; Chopdekar, R.; Jia, Y.; Wright, P.; et al. Electric Field-Induced Magnetization Switching in Epitaxial Columnar Nanostructures. *Nano Lett.* **2005**, *5*, 1793–96.
15. Levin, I.; Li, J.; Slutsker, J.; Roytburd, A. L. Design of Self-Assembled Multiferroic Nanostructures in Epitaxial Films. *Adv. Mater.* **2006**, *18*, 204447.
16. Gao, X. S.; Liu, L.; Lee, W.; Birajdar, B I.; Ziese, M.; Alexe, M.; Hesse, D. High-Density Periodically Ordered Magnetic Cobalt Ferrite Nanodot Arrays by Template-Assisted Pulsed Laser Deposition. *Adv. Funct. Mater.* **2009**, *19*, 3450–55.

17. Lee, W.; Han, H.; Lotnyk, A.; Schubert, M. A.; Senz, S.; Alexe, M.; Hesse, D.; Baik, S.; Gösele, U. Individually Addressable Epitaxial Ferroelectric Nanocapacitor Arrays with Near Tb $Inch^{-2}$ Density. *Nat. Nanotechnol.* **2008**, *3*, 402–07.
18. Liu, L.; Lee, W.; Huang, Z.; Scholz, R.; Gösele, U. Fabrication and characterization of a flow-through nanoporous gold nanowire/AAO composite membrane. *Nanotechnology* **2008**, *19*, 335604.
19. Li, A. P.; Müller, F.; Birner, A.; Nielsch, K.; Gösele, U. Hexagonal Pore Arrays with a 50−420 nm Interpore Distance Formed by Self-Organization in Anodic Alumina. *J. Appl. Phys.* **1998**, *84*, 6023–26.
20. Masuda, H.; Fukuda, K. Ordered Metal Nanohole Arrays Made by a Two-Step Replication of Honeycomb Structures of Anodic Alumina. *Science* **1995**, *268*, 1466–68.
21. Lee, W.; Ji, R.; Gösele, U.; Nielsch, K. Fast Fabrication of Long-Range Ordered Porous Alumina Membranes by Hard Anodization. *Nat. Mater.* **2006**, *5*, 741–47.
22. Rodriguez, B. J.; Gao, X. S.; Liu, L. F.; Alexe, M.; Hesse, D.; Lee, W.; Naumov, I. I.; Bratkovsky, A. M. Vortex Polarization States in Nanoscale Ferroelectric Arrays. *Nano Lett.* **2009**, *9*, 1127–31.
23. Choi, J.; Nielsch, K.; Reiche, R.; Wehrspohn, R. B.; Gösele, U. Fabrication of Monodomain Alumina Pore Arrays with an Interpore Distance Smaller Than The Lattice Constant of the Imprint Stamp. *J. Vac. Sci. Technol., B* **2003**, *21*, 763–66.
24. Cullity, B. D. *Introduction of Magnetic Materials*; Addison-Wesley: Reading, MA, 1972.
25. Gao, X. S.; Bao, D. H.; Birajdar, B.; Habisreuther, T.; Mattheis, R.; Schubert, M. A.; Alexe, M.; Hesse, D. Switching of Magnetic Anisotropy in Epitaxial $CoFe_2O_4$ Thin Films Induced by $SrRuO_3$ Buffer Layer. *J. Phys. D: Appl. Phys.* **2009**, *42*, 175006.
26. Lisfi, A.; Williams, C. M.; Nguyen, L. T.; Lodder, J. C.; Coleman, A.; Corcoran, H.; Johnson, A.; Chang, P.; Kumar, A.; Morgan, W. Reorientation Of Magnetic Anisotropy In Epitaxial Cobalt Ferrite Thin Films. *Phys. Rev. B* **2007**, *76*, 054405.
27. Maglione, M. Interface-Driven Magnetocapacitance in a Broad Range of Materials. *J. Phys. C* **2008**, *20*, 322202.
28. Catalan, G. Magnetocapacitance without Magnetoelectric Coupling. *Appl. Phys. Lett.* **2006**, *88*, 102902.